applied sciences

MDPI

Article

Numerical Analysis of Gravity Casting of a 34CrMo4 Steel Flywheel Rotor for Energy Storage Applications

Jana Růžička [1], Adéla Macháčková [1,*], Filip Radkovský [1] and Miroslav Trochta [2]

[1] Department of Metallurgical Technologies, Faculty of Materials Science and Technology, VSB—Technical University of Ostrava, 17. listopadu 2172/15, 70800 Ostrava, Czech Republic; jana.ruzicka@vsb.cz (J.R.); filip.radkovsky@vsb.cz (F.R.)

[2] Department of Machine Parts and Mechanisms, Faculty of Mechanical Engineering, VSB—Technical University of Ostrava, 17. listopadu 2172/15, 70800 Ostrava, Czech Republic; miroslav.trochta@vsb.cz

* Correspondence: adela.machackova@vsb.cz

Abstract

Flywheel energy storage systems impose high demands on the mechanical properties and structural integrity of rotors, particularly in high-speed applications. This study focuses on the numerical analysis of gravity casting of a steel rotor manufactured from low alloy 34CrMo4 steel, with the aim of identifying critical regions related to molten metal flow, solidification behaviour and shrinkage defect formation. Numerical simulations were calculated using a MAGMASOFT® 5.5 software environment based on the finite volume method and included both mold filling and subsequent solidification and cooling stages. Flow stability, temperature field distribution and solidification characteristics were researched thoroughly. The results showed that optimization of the gating and feeding system lowered porosity under 2% within the casting and relocated shrinkage defects to the risers. At the same time, solidification directionality was improved and the Hot Spot value was reduced. From the perspective of casting quality, the proposed design represents the most suitable solution, despite a lower metal utilization rate. The analysed casting forms the structural body of a hybrid flywheel rotor intended for the subsequent integration of high-density tungsten segments.

Keywords: flywheel energy storage system (FESS); steel casting; MAGMASOFT®; solidification; porosity; feeding system; casting optimization; hot spot

1. Introduction

Flywheel Energy Storage Systems (FESSs) represent a promising energy storage technology characterized by high efficiency, long service life and the ability to rapidly store and release energy. FESSs can deliver high power outputs with short response times and complement conventional electrochemical batteries due to their low degradation rate and environmentally friendly operation [1,2].

The rotor is the most critical component from both a structural and safety perspective. It must withstand extreme centrifugal forces generated during high-speed operation while maintaining sufficient resistance to fatigue damage and sudden failure. Rotor failure represents one of the most severe risks associated with flywheel energy storage. Therefore, the design of rotor geometry, material selection and manufacturing technology is essential for ensuring overall system reliability [3].

The energy storage capacity of a flywheel is directly proportional to its moment of inertia and the square of its angular velocity. Consequently, current research focuses not

Check for updates

Received: 16 June 2026
Revised: 9 July 2026
Accepted: 13 July 2026
Published: 15 July 2026

 https://doi.org/10.3390/app16147080

only on high-speed composite rotors but also on robust metallic designs that combine high material density with good mechanical integrity. Steel rotors remain attractive for applications requiring long-term operational stability, high mechanical resistance and economic feasibility [4–6].

Low-alloy chromium–molybdenum steel 34CrMo4 is a well-established structural material used for components subjected to high mechanical loads. Its combination of high strength, toughness, hardenability and fatigue resistance makes it suitable for large rotating components, including rotors for energy storage systems [7].

However, the production of large cast components from this steel is associated with an increased risk of internal defects, particularly porosity, segregation and other structural discontinuities. Such defects may significantly reduce the mechanical integrity and operational reliability of the final casting. This issue is especially critical for FESS rotors, where even local material discontinuities may initiate fatigue cracks or lead to catastrophic failure during operation [8,9]. The prediction and elimination of casting defects require a detailed understanding of the physical phenomena occurring during mold filling and solidification. For this reason, numerical simulation has become a standard tool for the design and optimization of foundry processes. These simulations enable the analysis of molten metal flow, heat transfer, solidification behaviour and potential defect formation before actual production, thereby reducing experimental costs and improving casting quality [10,11]. Advanced software packages such as MAGMASOFT® integrate comprehensive physical models of fluid flow, heat transfer and phase transformations. These tools enable the optimization of gating and feeding systems, solidification control and overall technological conditions for steel castings [12,13].

Current trends in FESS development focus not only on optimizing manufacturing processes but also on innovative rotor concepts that increase energy density without a disproportionate increase in mechanical risk. One promising approach is the hybrid rotor concept, which combines a steel structural body with locally integrated high-density segments positioned in regions contributing most effectively to the moment of inertia [2,14].

The flywheel proposed in this study is designed as a hybrid rotor for FESS applications. It combines a steel casting made of 34CrMo4 steel with integrated high-density segments based on tungsten heavy alloys. The primary design objective is to increase the rotor moment of inertia while maintaining mechanical integrity, dynamic stability and manufacturing feasibility.

The steel casting serves as the primary load-bearing structure and transfers the mechanical loads generated during rotation. High-density tungsten alloy segments are integrated into precisely defined locations within the steel body. Owing to their exceptionally high density, these segments significantly enhance the energy storage capacity of the flywheel. Their geometry enables a smooth mass distribution along the rotor circumference and minimizes stress concentrations at material interfaces.

Although numerical optimization of steel castings has been extensively reported, no studies have addressed the casting technology of a hybrid flywheel rotor containing multiple internal cavities intended for the subsequent integration of tungsten heavy-alloy segments. The present work therefore investigates how this unconventional geometry influences mould filling, solidification behaviour and shrinkage defect formation, and proposes a technological solution enabling the manufacture of this novel rotor concept.

The tungsten segments are based on W–Ni–Co and W–Ni–Fe alloys, which exhibit high density and favourable mechanical properties. Their primary function is to increase the moment of inertia of the hybrid rotor. An additional advantage of the proposed concept is the possibility of utilizing recycled tungsten alloys, contributing to more efficient use of critical raw materials and supporting circular economy principles [1,2].

https://doi.org/10.3390/app16147080

The integration of a steel casting with tungsten composite segments increased demands on geometric design, manufacturing tolerances and process compatibility. The physical and thermomechanical properties of steel require a detailed analysis of the casting process, particularly in regions intended for the future placement of tungsten segments. Numerical casting simulations therefore represent a key tool for evaluating temperature fields, solidification behavior and the risk of internal defect formation.

The aim of this study is to perform a numerical analysis of the gravity casting process of a 34CrMo4 steel flywheel rotor, focusing on mold filling, temperature distribution, solidification behavior and porosity formation. Based on the simulation results, recommendations are proposed for optimizing the gating system and technological conditions to improve casting quality and enhance the operational reliability of FESS rotors intended for subsequent integration with high-density tungsten segments.

The scientific contribution of this work is not numerical optimization itself, which represents an established engineering approach, but its application to an originally designed hybrid flywheel rotor containing eight internal cavities intended for the subsequent integration of tungsten heavy-pseudoalloy segments. Such geometry introduces specific solidification conditions that have not been reported for FESS steel rotor castings. FESSs with this specific rotor structure are a specific problem and require specific solutions.

2. Materials and Methods

2.1. Material for Numerical Simulation

Low-alloy chromium–molybdenum steel 34CrMo4 (EN 1.7220; germany) belongs to the group of structural steels intended for applications subjected to high mechanical loading, where a combination of high strength, toughness and operational reliability is required. The presence of chromium and molybdenum improves the hardenability of the steel and enables the achievement of homogeneous mechanical properties even in large cross-sectional components [15].

After appropriate heat treatment, 34CrMo4 steel exhibits a tensile strength ranging from 800 to 1000 MPa while maintaining sufficient toughness and wear resistance. These properties make it suitable for shafts, highly stressed rotating components, pressure systems and other structural parts exposed to cyclic loading [16–19].

The microstructure of 34CrMo4 steel is heavily influenced by heat treatment. Quenching and tempering result in the formation of a fine-grained martensitic structure, which contributes to high strength, toughness and favourable fatigue properties [16,17]. The steel also exhibits good corrosion resistance under standard operating conditions and its properties can be further enhanced by suitable surface treatments [17,20,21]. Owing to its combination of mechanical performance and operational reliability, 34CrMo4 steel is widely used in mechanical engineering, power engineering and other applications subjected to high mechanical and fatigue loading [22].

For the numerical simulations of gravity casting performed in this study, 34CrMo4 (EN 1.7220) steel was selected as a representative material for highly loaded rotating components, specifically flywheel rotors used in Flywheel Energy Storage Systems (FESSs). Within the MAGMASOFT® material database, this alloy is designated as GS-34CrMo4. The material data used in the simulations included temperature-dependent thermophysical properties such as density, specific heat capacity, thermal conductivity, latent heat of solidification and liquid-phase viscosity. The chemical composition of the alloy complies with the relevant standard requirements and is presented in Table 1.

Table 1. Chemical composition of 34CrMo4 steel used for numerical simulations (wt. %) [23].

Element	C	Si	Mn	P	S	Cr	Mo
wt. %	0.340	0.400	0.650	0.020	0.015	1.000	0.375

2.2. Scope of the Numerical Simulation

The numerical simulation presented in this study is exclusively focused on the gravity casting process of a steel flywheel rotor. The simulated model includes only the steel casting and the associated technological elements, namely the gating system, risers and mould assembly.

The multimetallic heavy segments based on tungsten heavy alloys (e.g., W–Ni–Co and W–Ni–Fe), which are incorporated into the final rotor design to increase its moment of inertia, are not included in the numerical model and do not enter any stage of the mould filling, solidification, or cooling simulations. These segments are considered independent prefabricated components that are integrated into the steel rotor body only during the subsequent assembly stage.

For this reason, tungsten heavy alloys were not included in the MAGMASOFT® material database and their thermophysical and rheological properties were not considered within the scope of this study.

Although the tungsten segments are not part of the numerical model, they constitute an integral component of the proposed hybrid rotor concept. Their presence influenced the casting design, particularly the geometry of the internal cavities intended for their subsequent installation. Therefore, the basic characteristics of the tungsten heavy alloys used are briefly summarized in Appendix A.

2.3. Rotor Geometry and Simulation Input Parameters

The geometry of the rotor was developed based on a detailed technical drawing corresponding to the manufactured component. The introductory figures show the casting after final machining. The rotor is fully rotationally symmetric about its central axis, ensuring uniform mass distribution and minimizing geometric eccentricity. All dimensions used for numerical modelling were taken directly from the design documentation without scaling modifications or geometric simplifications.

The proposed design represents an original hybrid rotor concept incorporating heavy segments. The design is intended to optimize mass distribution and improve the mechanical performance of the rotor while maintaining manufacturing feasibility. For the purposes of numerical simulation, a three-dimensional model corresponding to the casting geometry was created. This model was subsequently used as the input geometry for casting simulations performed in the MAGMASOFT® software environment.

The overall height of the actual rotor is 321 mm, as shown in the longitudinal section presented in Figure 1. The central part of the rotor, which forms the main load-bearing region of the structure, has an axial thickness of 174 $\pm$ 0.05 mm. This section connects the upper and lower bearing seats and simultaneously contains radially distributed internal cavities intended for the subsequent installation of tungsten heavy-alloy segments. The smooth transitions between the central body and the bearing regions follow the geometry defined in the technical drawing and play an important role in minimizing notch effects and reducing stress concentration during operation.

https://doi.org/10.3390/app16147080

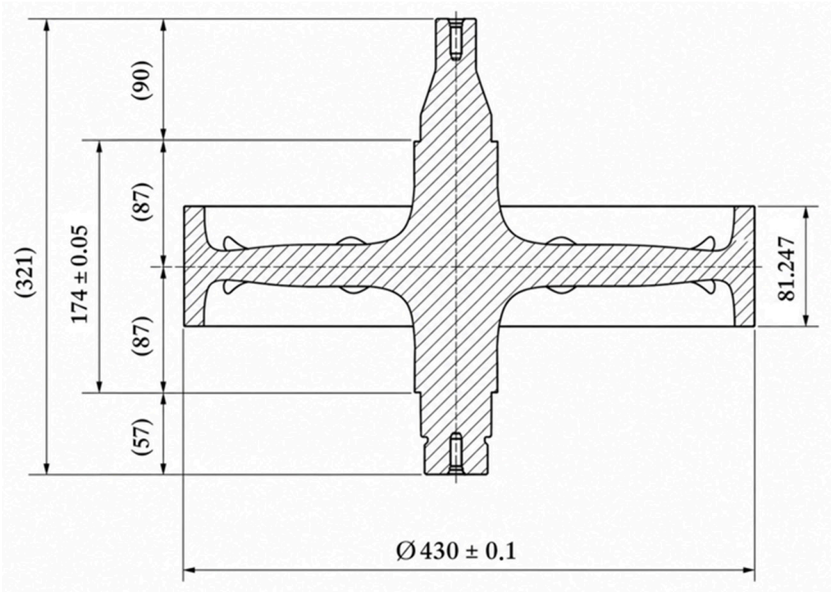

Figure 1. Longitudinal cross-section of the rotor.

The geometry of the bearing region is shown in detail in the side view presented in Figure 2. The upper and lower sections have the same diameter in the bearing seating area; however, the remaining design features differ. In the upper section, the bearing diameter is followed by a tapered transition region with machined flats intended for torque transmission during the tightening of the retaining nut. This region is followed by a cylindrical shaft end used to transmit torque during the acceleration and deceleration of the flywheel. In the lower section, the bearing diameter is followed by a threaded portion designed for a retaining nut that secures the bearings on the shaft.

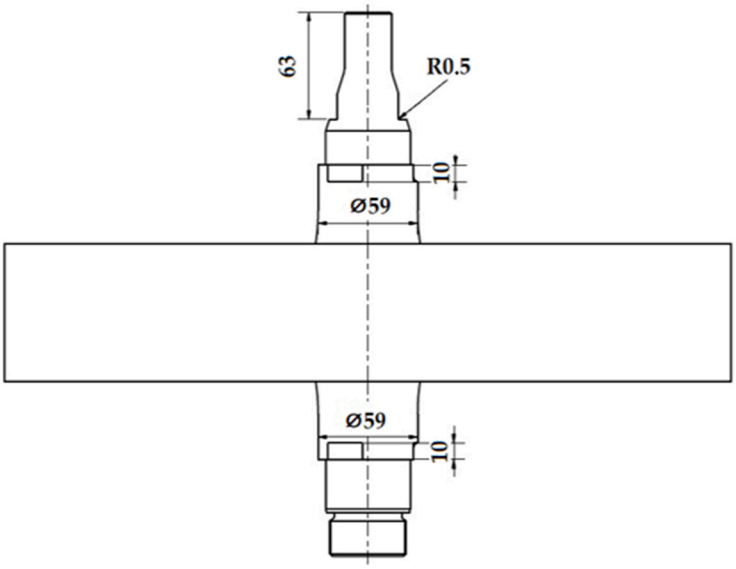

Figure 2. Side view of the rotor.

The outer diameter of the rotor is Ø430 $\pm$ 0.1 mm, as shown in the front view presented in Figure 3. The rotor body contains eight internal cavities uniformly distributed around the circumference. The cavities are arranged with a constant angular spacing of 45°, while their axes are rotated by 22.5° relative to the principal coordinate axes. The cavities exhibit a characteristic teardrop-shaped geometry designed to maximize the effective use of the available space intended for the future installation of tungsten heavy-alloy segments while preserving the continuity of the load-bearing rotor structure. In addition, this geometry enables a more efficient distribution of mass to regions located farther from the axis of rotation, thereby contributing to an increase in the rotor moment of inertia.

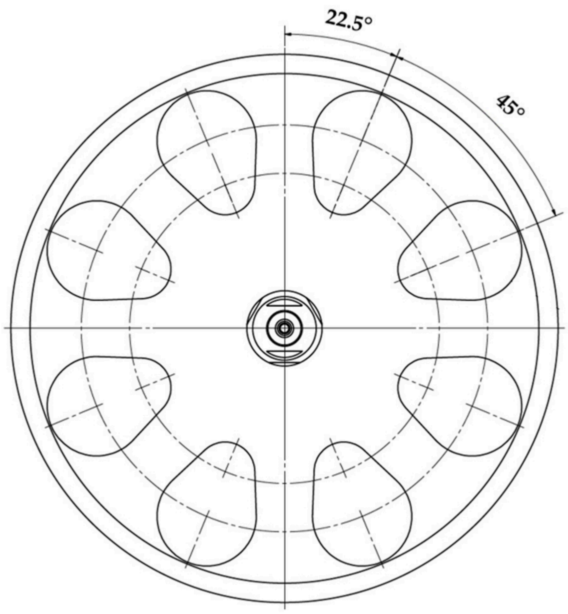

Figure 3. Front view of the rotor.

For the purposes of numerical simulation, all geometric features directly affecting the volume, mass distribution and rotational characteristics of the rotor were retained. Dimensional tolerances specified in the technical drawing were considered for the key dimensions. The resulting geometry was implemented as a fully parametric three-dimensional solid model and subsequently used as the input geometry for the numerical casting simulations.

3. Results

The final variant of the rotor was its ninth iteration. Previous variants were excluded because their numerical simulations were considered unsuitable due to a high percentage of various defects. The main focus of enhancements from v01 to v08 was to improve the flow of the melt trough runner system.

3.1. Numerical Mesh of the Casting Variant v09

The gating system was designed and modelled directly in the MAGMASOFT® simulation environment. The complete numerical model of the casting was discretized using a computational mesh consisting of 65,600 cells, as shown in Figure 4. The casting process was simulated using a sand mould composed of a bentonite-bonded moulding mixture. The mould system was supplemented with feeder insulation sleeves and steel chills made of common structural steel to control the solidification process. The pouring temperature was set to 1600 °C, while the filling time was automatically controlled by the internal MAGMASOFT® algorithm. The computation time for a single simulation variant was approximately 16 min. The net weight of the casting was 33.79 kg, whereas the total weight including the gating and feeding system reached 44.37 kg. Based on these values, the metal yield was calculated to be 76.15%. This value falls within the upper range typically reported for steel castings (approximately 60–80%), indicating an efficient gating and feeding system design while maintaining the technological requirements necessary to ensure casting quality.

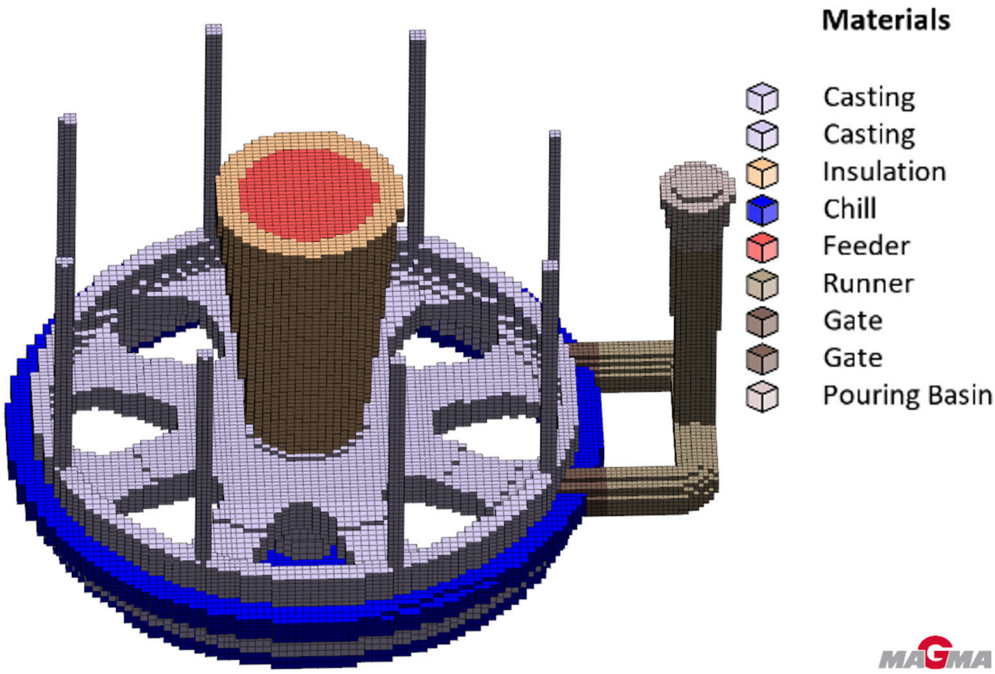

Figure 4. Numerical mesh of the casting variant v09.

3.2. Temperature Field During Mold Filling—Variant v09

Figure 5 shows the temperature distribution of the molten metal during the mould filling stage at 8.219 s after the start of pouring. At this time, the casting cavity, including the gating and feeding system, is completely filled. The temperature ranges from 1485 °C to 1600 °C.

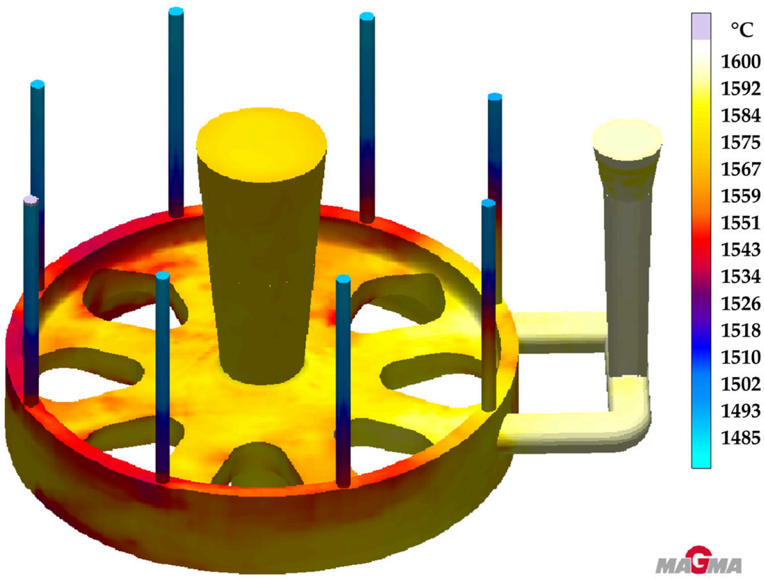

Figure 5. Surface temperature distribution for variant v09.

The highest temperatures are concentrated within the gating system and in the region of the central riser. These areas are characterized by the inflow of freshly poured molten metal and a larger metal volume. In contrast, lower temperatures were observed in the thin-walled regions of the outer ring and ribs due to more intensive heat transfer to the mould.

The central part of the casting and the riser maintain a higher temperature level throughout the subsequent stages of solidification. This creates favourable conditions for compensating volumetric shrinkage during solidification. At the same time, these regions represent potential locations for the formation of internal defects.

The temperature field does not exhibit significant undercooled regions. Therefore, the risk of premature solidification of the molten metal is low. The smooth temperature distribution confirms stable mould filling conditions and an appropriately designed gating system.

3.3. Evolution of the Minimum Temperature During Casting—Variant v09

Figure 6 shows the evolution of the minimum molten metal temperature during the mould filling stage. The curve illustrates the decrease in temperature from the initial pouring temperature of approximately 1600 °C to lower values as a result of heat transfer to the mould and the increasing contact time between the molten metal and the mould cavity.

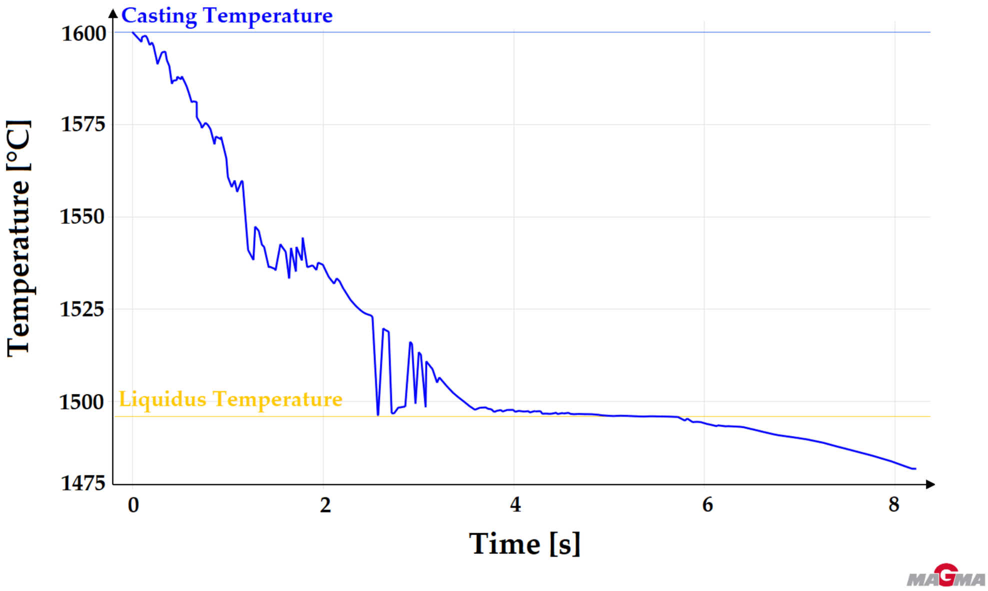

Figure 6. Minimum molten metal temperature during casting for variant v09.

During the first second of the process, a rapid decrease in the minimum temperature is observed as a result of the contact between the molten metal and the colder mould. Between approximately 1.5–3 s, temperature fluctuations occur due to transient flow conditions and the filling of more complex geometric features.

At approximately 3–4 s, the minimum temperature approaches the liquidus temperature. Subsequently, the rate of temperature decrease slows down and the curve gradually stabilizes, indicating progressive homogenization of the temperature field within the casting. After approximately 5 s, when the vent channels and the riser are being filled, an additional slight temperature decrease can be observed.

After the completion of mould filling at 8.219 s, the minimum temperature continues to decrease gradually, reaching approximately 1475 °C at the end of the monitored interval. The temperature profile does not indicate significant undercooling during mould filling, suggesting stable thermal conditions and a low risk of cold shuts or misruns.

3.4. Solidification Modulus of Casting—Variant v09

Figure 7 shows the distribution of the solidification modulus within the casting–gating–feeding system during the solidification and cooling stages. The highest modulus values, approximately 2.749 cm, are located in the region of the central riser and along the central axis of the casting. These regions solidify last and provide feeding to compensate for volumetric shrinkage during solidification. In contrast, the outer ring and thin-walled sections exhibit lower modulus values of approximately 0.620 cm, corresponding to their faster solidification rate.

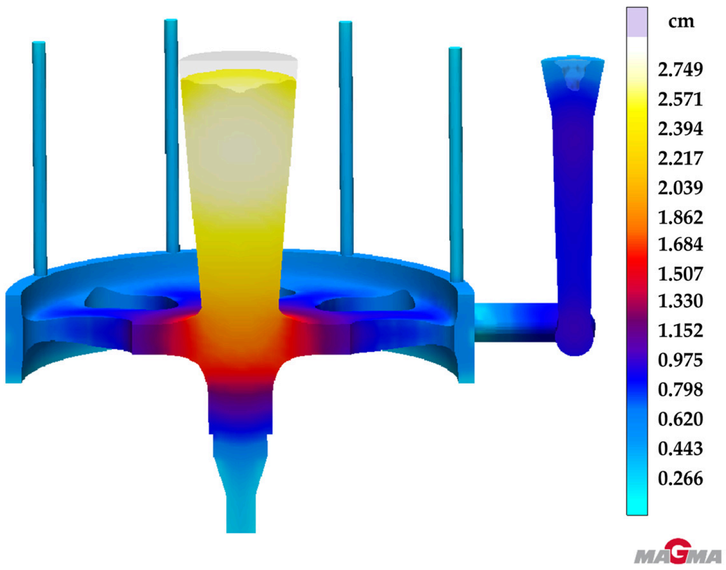

Figure 7. Solidification modulus distribution in casting variant v09.

The modulus distribution indicates directional solidification toward the central riser. These regions may also act as locations for the concentration of internal defects and non-metallic inclusions transported from the previously solidified sections of the casting.

3.5. Hot Spot Distribution in Casting—Variant v09

Figure 8 illustrates the distribution of the Hot Spot criterion during the solidification and cooling stages of casting variant v09. These are the areas of cumulation of the melt with the highest temperature. Hot Spots are to be eliminated or driven out of the body of the final casting. The highest values are located in the region of the central riser, particularly in its upper section, where the longest solidification time of up to 1948 s is predicted. This region represents the last solidifying part of the casting system.

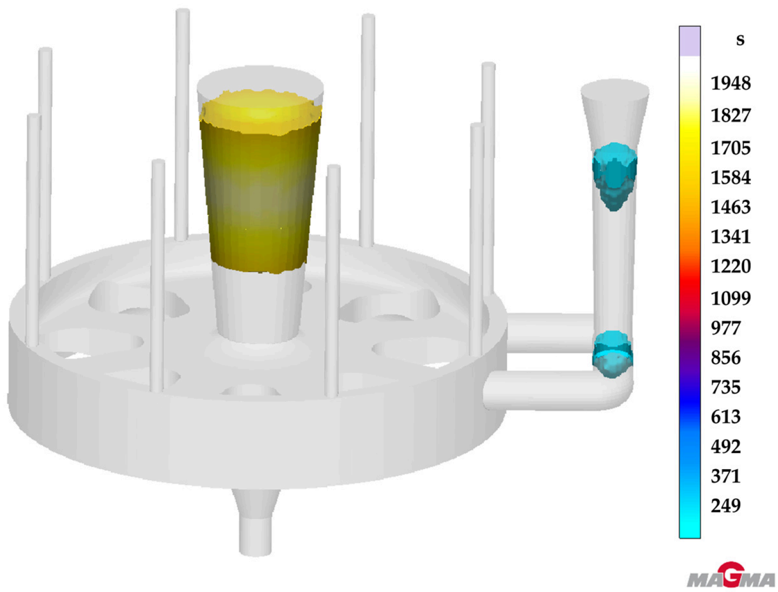

Figure 8. Hot Spot distribution in casting variant v09.

Secondary hot spots are identified within the gating system. Their formation is associated with locally increased metal volume and reduced heat dissipation.

The remaining parts of the casting, including the outer ring and ribs, solidify earlier and therefore do not represent critical regions with respect to shrinkage defect formation.

3.6. Total Porosity Distribution in Casting—Variant v09

Figure 9 shows the overall porosity distribution within the selected cross-section of the numerical model. The maximum predicted porosity value of 100% is located in the riser region and does not extend into the casting itself. Within the casting, porosity occurs only locally, primarily in the thin-walled sections of the outer ring and in the vicinity of the cavities intended for the subsequent installation of tungsten heavy-alloy segments. Porosity is located at junction points or at the places where multiple faces meet. Here a separation of a minuscule dose of liquid metal occurs. The solidification of these places is occurring separated from the main body which leads to shrinkage outside of the riser. The maximum porosity level predicted within the casting is approximately 7.5%.

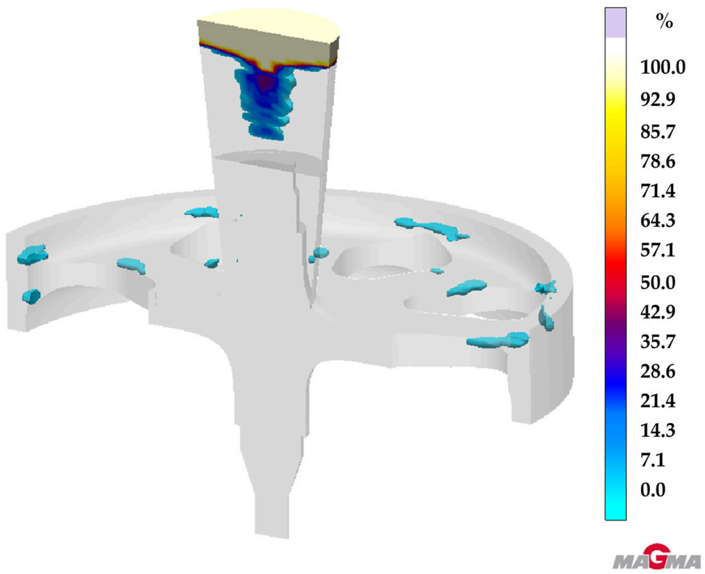

Figure 9. Total porosity distribution in casting variant v09.

From a technological perspective, the predicted porosity level is relatively low. However, its distribution indicates potential for further optimization of the gating and feeding system in order to minimize the formation of internal defects and promote a more uniform solidification process.

3.7. Pore Volume Distribution in Casting—Variant v09

Figure 10 presents the distribution of pore volume within the casting. The largest predicted pore volume is concentrated in the riser, where it reaches a value of 2.0483×10^5 mm^3. In the remaining parts of the casting, only small and isolated pore volumes are predicted. Despite their limited size, these local pores may significantly affect the operational reliability of the component. They represent potential sites for crack initiation, contribute to a reduction in rotor fatigue life, and may adversely affect dynamic balancing, resulting in increased vibration levels during operation. Cavities are to be limited or minimized; in this casting, they are due to shrinkage. Therefore, the minimization of such defects remains an important objective and requires further optimization of both the technological parameters and the gating and feeding system design.

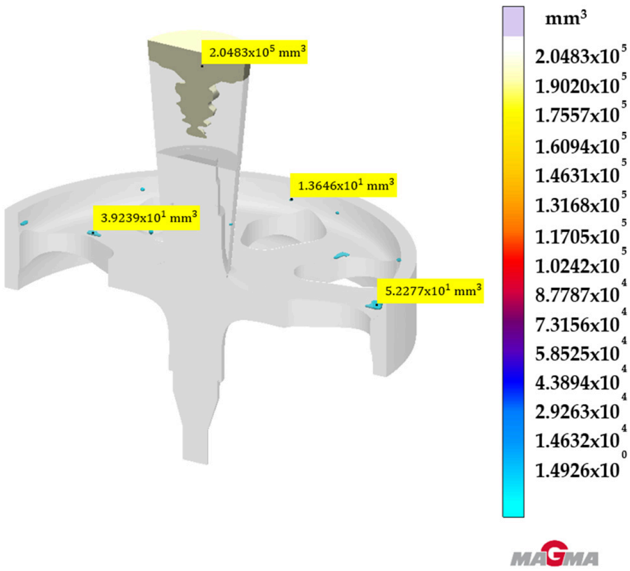

Figure 10. Pore volume distribution in the casting version v09.

3.8. Development and Optimization of Numerical Models for Casting Variants v10–v13

Figure 11 presents the numerical models of casting variants v10–v13, which differ in the application of technological measures aimed at controlling solidification and reducing porosity formation.

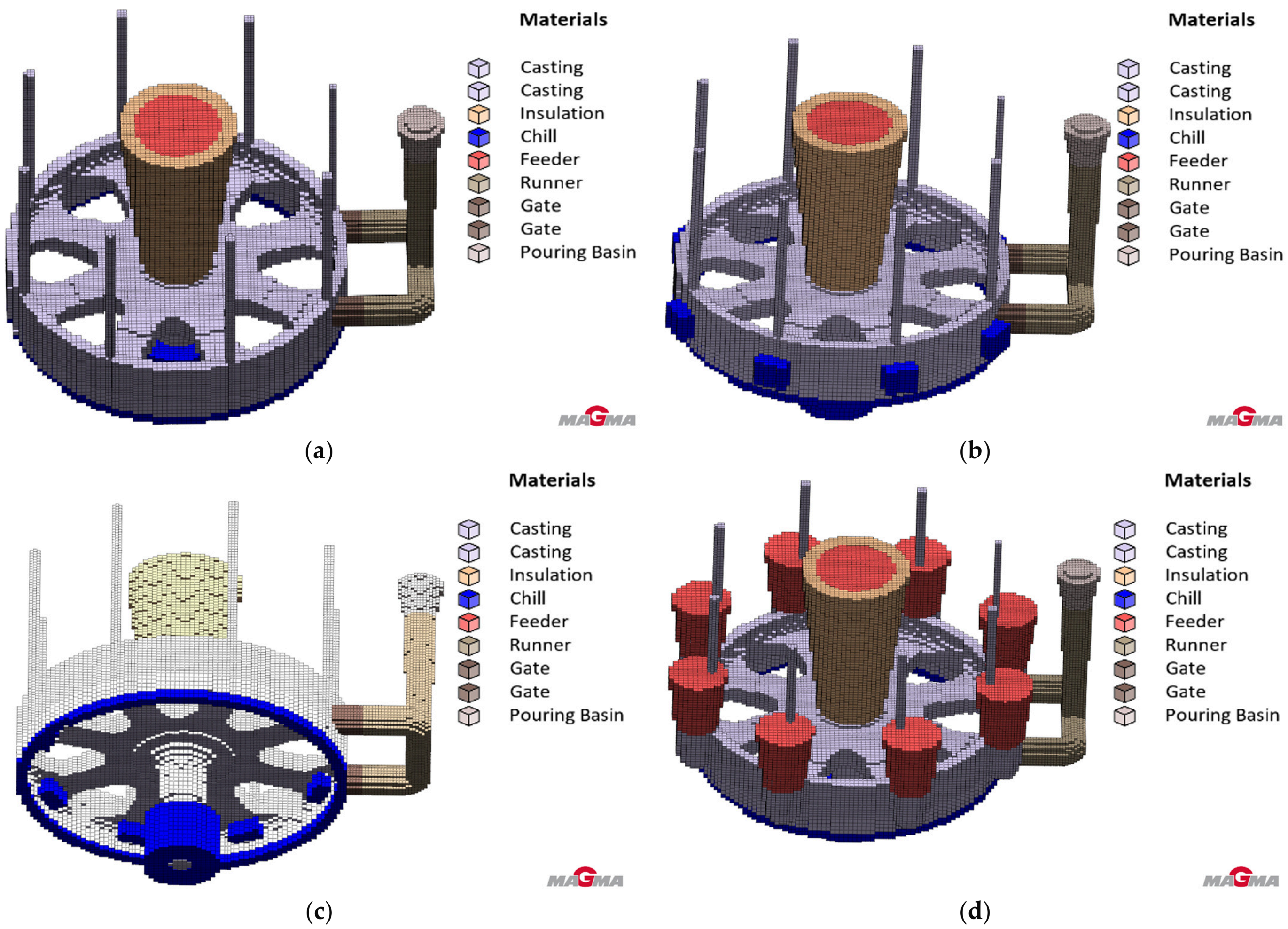

Figure 11. Numerical models of casting variants: (**a**) v10; (**b**) v11; (**c**) v12; (**d**) v13.

Variant v10 (Figure 11a) was designed without an external chill ring. This configuration resulted in an unfavourable solidification pattern and increased porosity, particularly in the regions where the spokes (ribs) are connected to the outer ring.

In variant v11 (Figure 11b), chills were positioned on the outer side of the spokes. This modification led only to a slight improvement and porosity remained present in the critical regions.

In variant v12 (Figure 11c), chills were applied to the bottom side of the rib-to-ring transition area. This measure altered the solidification behaviour and shifted the porosity toward the upper part of the outer ring, but porosity is still present.

Variant v13 (Figure 11d) included the addition of risers. Although this modification increased the technological complexity of the casting process, it resulted in the most significant reduction in porosity.

The simulations were performed at a pouring temperature of 1600 °C. The computation time for a single simulation variant was approximately 20 min. The numerical model was discretized using a computational mesh consisting of 99,066 cells. The net casting weight was 38.94 kg, while the total weight including the gating and feeding system reached 67.38 kg, corresponding to a metal yield of 57.79%. For steel casts of this volume, it is still within the boundaries of acceptance.

The progressive modifications introduced in the individual variants reflect an effort to optimize the casting technology and achieve stable solidification conditions with a minimal occurrence of internal defects.

3.9. Temperature Field During Mould Filling—Variant v13

Figure 12 illustrates the temperature distribution of the molten metal during the mould filling stage 8.35 s after the start of pouring. The temperature field corresponds to the moment when the casting cavity, including the gating and feeding system, is completely filled. The colour scale represents temperatures ranging from approximately 1501–1600 °C. The highest temperatures are concentrated within the gating system, the adjacent massive sections of the casting, and the central riser.

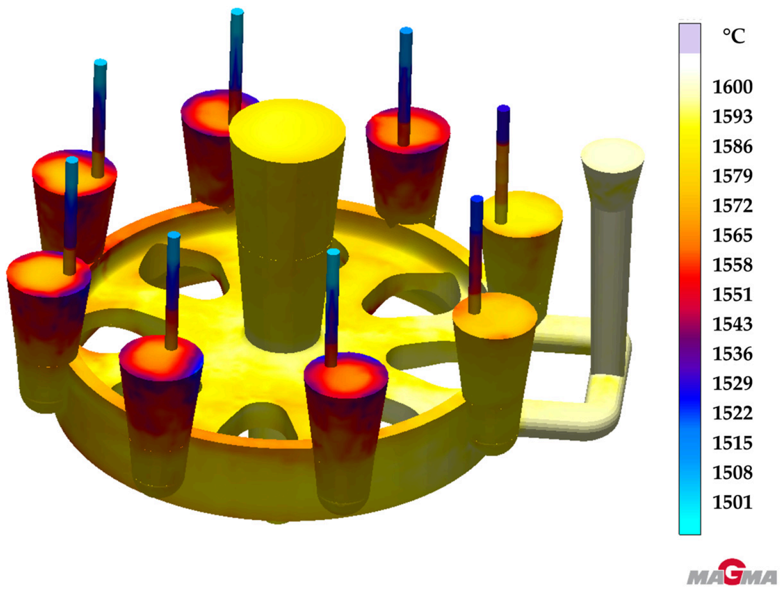

Figure 12. Surface temperature distribution at the end of mold filling for variant v13.

3.10. Evolution of the Minimum Temperature During Casting—Variant v13

Figure 13 shows the evolution of the minimum molten metal temperature during the mould filling stage. The temperature decreases from the initial pouring temperature of 1600 °C as a result of heat transfer to the mould. At approximately 4–5 s, the curve approaches the liquidus temperature of about 1495 °C, after which the rate of temperature decrease becomes less pronounced.

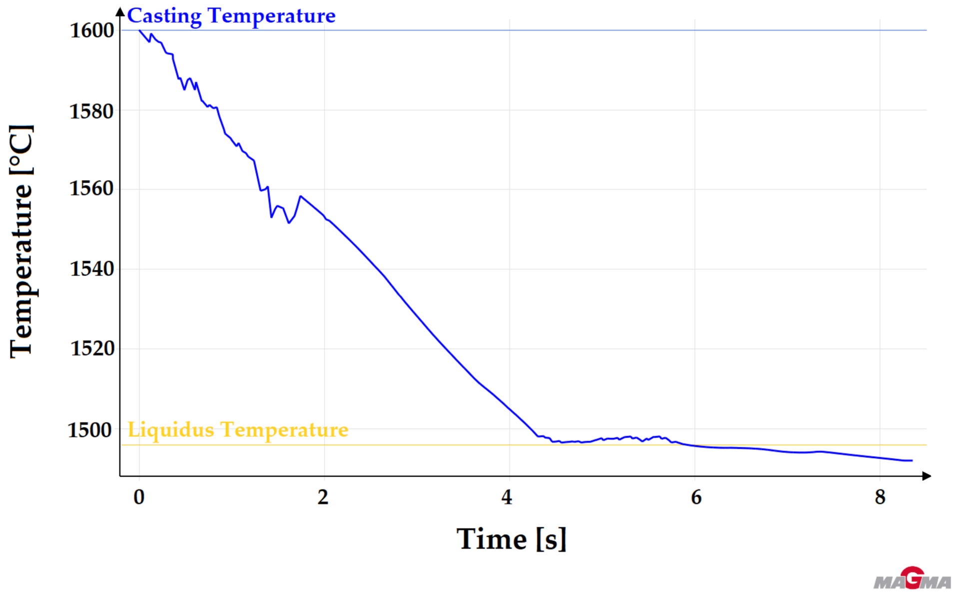

Figure 13. Evolution of the minimum molten metal temperature during casting for variant v13.

3.11. Solidification Modulus of Casting—Variant v13

Figure 14 shows the distribution of the solidification modulus within the casting–gating–feeding system during the solidification and cooling stages. The highest modulus values, approximately 2.759 cm, are located in the region of the central riser and along the central axis of the casting. These regions solidify last and provide feeding to compensate for volumetric shrinkage during solidification. In contrast, the outer ring and thin-walled sections exhibit lower modulus values of approximately 0.452 cm, corresponding to their faster solidification rate.

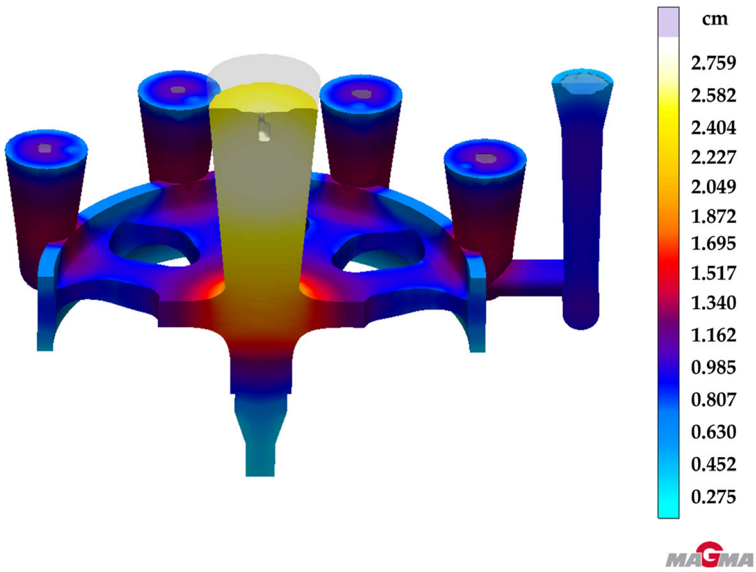

Figure 14. Solidification modulus distribution in casting variant v13.

3.12. Hot Spot Distribution in Casting—Variant v13

Figure 15 illustrates the distribution of the Hot Spot criterion during the solidification and cooling stages of casting variant v13. The highest value, approximately 1778 s, is located in the region of the central riser, which represents the last solidifying part of the casting system.

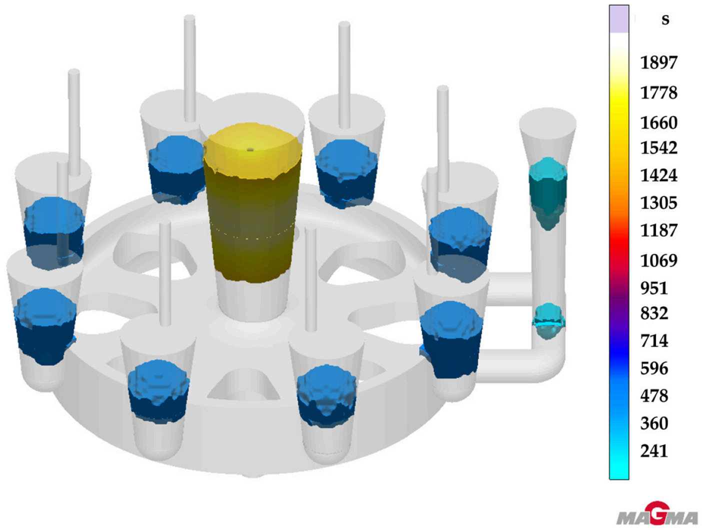

Figure 15. Hot Spot distribution in casting variant v13.

Secondary hot spots are identified in the peripheral risers and, to a lesser extent, within the gating system. These regions exhibit longer solidification times due to their larger metal volume. Hot Spots are moved to the side or outside of the casting, which is desirable and common practice.

3.13. Total Porosity Distribution in Casting—Variant v13

Figure 16 illustrates the distribution of total porosity in casting variant v13. The highest porosity values are located in the region of the central riser. Within the casting itself, porosity occurs only locally in the form of small, isolated cavities, primarily in transition regions. These porosity levels are significantly lower than those observed in previous variants, do not exceed 2% in blue areas and do not form continuous volumetric concentrations.

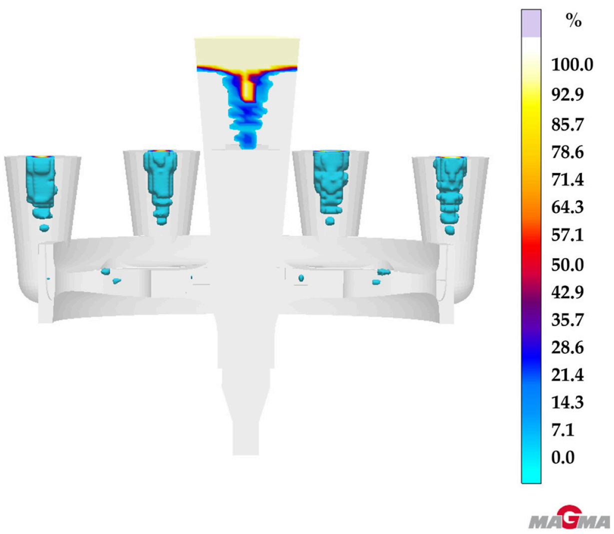

Figure 16. Total porosity distribution in casting variant v13.

The porosity distribution corresponds to directional solidification toward the risers, with the majority of defects concentrated outside the functional regions of the casting. Risers are removed and, with them, a marginal volume of porosity is removed as well.

3.14. Pore Volume Distribution in Casting—Variant v13

Figure 17 presents the distribution of pore volume within the casting. The highest value, approximately 2.9069×10^5 mm^3, is located in the central riser region. No pore volume was detected within the casting itself. The predicted pore volumes are concentrated exclusively within the central riser and the peripheral risers.

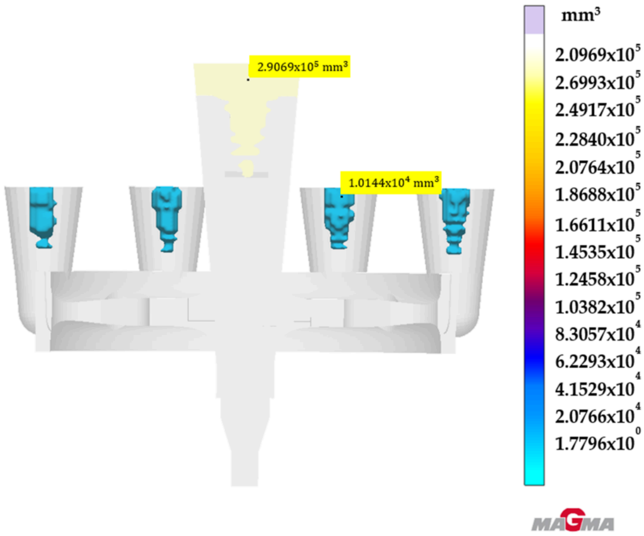

Figure 17. Pore volume distribution in casting variant v13.

The pore volume distribution confirms directional solidification toward the risers, with volumetric defects effectively transferred outside the functional part of the casting.

Variant v13 was therefore selected as the recommended technological solution for rotor production.

4. Discussion

The comparison of variants v09 and v13 presented in Table 2 demonstrates that modifications to the gating and feeding system improved both the solidification behaviour and the porosity distribution. Variant v09 exhibited local porosity within the casting of up to approximately 7.5%, whereas in variant v13 porosity was detected exclusively within the risers, with no porosity identified in the casting itself. At the same time, the maximum Hot Spot value decreased from approximately 1948 s to 1778 s, indicating more effective solidification control and improved feeding conditions.

The improvement achieved in variant v13 is associated with the modification of the feeding system, which enabled more effective control of directional solidification. The additional risers provided a sufficient supply of liquid metal during solidification and promoted the transfer of volumetric defects outside the functional part of the casting. This effect is evident from the temperature field distribution, the solidification modulus distribution, and the localization of Hot Spots.

From the perspective of technological design, this represents a typical trade-off between casting quality and metal yield. Variant v13 exhibited a lower metal yield of 57.79% compared with 76.15% for variant v09. This reduction resulted from the application of additional risers, which increased the weight of the gating and feeding system and the subsequent machining requirements. Nevertheless, this approach is justified because it enables the elimination of internal defects within the casting.

Table 2. Comparison of casting variants v09 and v13.

Parameter/Characteristic	Variant v09	Variant v13
Computational mesh (number of cells)	65,600	99,066
Pouring temperature (°C)	1600	1600
Computation time (min)	16	20
Casting weight (kg)	33.79	38.94
Total weight—including gating system (kg)	44.37	67.38
Metal yield (%)	76.15	57.79
Temperature field	Homogeneous	Homogeneous
Minimum temperature (°C)	1475	1495
Maximum solidification modulus (cm)	2.749	2.759
Minimum solidification modulus (cm)	0.620	0.452
Maximum Hot Spot (s)	1948	1778
Hot Spot location	Central riser and gating system	Central and peripheral risers
Total porosity (%)	7.5% within the casting	<2%, local occurrence
Pore volume distribution	Small pore volumes in the casting and riser	Restricted to risers only
Casting condition	Defects present within the casting	No porosity detected within the casting
Technological complexity	Lower	Higher (additional risers)
Recommended application	Alternative design	Recommended design

From an operational perspective, the reduction in porosity is of critical importance. Even small pores may act as crack initiation sites, reduce fatigue life and adversely affect the dynamic balancing of the rotor, leading to increased vibration levels. Therefore, the elimination of porosity within the casting itself represents a key factor in improving component reliability and service life.

Based on the performed analysis, variant v13 can be considered the most suitable solution in terms of porosity minimization and solidification control. The proposed configuration ensures the effective transfer of volumetric defects outside the functional part of the casting and provides stable solidification conditions, albeit at the cost of increased technological complexity.

For the final design, the pouring temperature was further examined. In addition to the pouring temperature of 1600 degrees, additional simulations were carried out for other temperatures. Thanks to this, it was found that the safe range of pouring temperatures is between 1590 and 1610 degrees without negatively affecting the casting.

Study Limitations

The presented results are based exclusively on numerical simulations performed using the MAGMASOFT® software environment. The extended mathematical simulations were performed for this specific steel. But the experimental cast was made using a different kind of ferrous material with comparable physical properties. This casting was done using a reduced model. Experimental validation of the simulation results on a real casting was not available at the time of this study. Furthermore, the tungsten heavy-alloy segments intended for subsequent integration into the hybrid rotor were not included in the numerical analysis, as they are not part of the casting process of the investigated steel rotor body.

5. Conclusions

This study focused on the numerical analysis of the casting process of a steel rotor intended for the subsequent integration of heavy segments. The primary objective was to optimize the gating and feeding system and minimize the occurrence of internal defects. Several technological variants were evaluated with respect to their influence on solidification behaviour and porosity formation.

The results showed that the original variant v09 exhibited local porosity within the casting of up to approximately 7.5%, particularly in transition regions. By modifying the gating and feeding system in variant v13, porosity within the casting was eliminated and transferred to the risers. At the same time, a reduction in the maximum Hot Spot value and an improvement in directional solidification were achieved.

Variant v13 was associated with a reduced metal yield of 57.79%, representing a technological trade-off between casting quality and production efficiency. Nevertheless, this approach is justified because the elimination of internal defects has a significant impact on the operational reliability, fatigue life and dynamic behaviour of the rotor.

The results demonstrate that optimization of the gating and feeding system is an effective tool for controlling the solidification process and minimizing porosity. Variant v13 represents the most suitable solution from the perspective of casting quality, despite its higher technological complexity.

Author Contributions: Conceptualization, J.R. and A.M.; methodology, F.R. and J.R.; software, F.R. and J.R.; validation, A.M., J.R. and F.R.; formal analysis, J.R.; investigation, J.R. and F.R.; resources, J.R.; data curation, J.R.; writing—original draft preparation, J.R.; writing—review and editing, J.R. and A.M.; visualization, J.R. and M.T.; supervision, A.M. and M.T.; project administration, J.R.; funding acquisition, A.M. All authors have read and agreed to the published version of the manuscript.

Funding: This research received no external funding.

Institutional Review Board Statement: Not applicable.

Informed Consent Statement: Not applicable.

Data Availability Statement: The original contributions presented in this study are included in the article. Further inquiries can be directed to the corresponding author.

Acknowledgments: This article has been elaborated in the framework of the grant programme "Support for Science and Research in the Moravia-Silesia Region 2025" (RRC/12/2025), financed from the budget of the Moravian-Silesian Region.

Conflicts of Interest: The authors declare no conflicts of interest.

Abbreviations

The following abbreviations are used in this manuscript:

FESS	Flywheel Energy Storage System

Appendix A

This appendix summarizes the basic material characteristics of W–Ni–Co and W–Ni–Fe tungsten heavy alloys, which are incorporated into the final rotor design in the form of heavy segments to increase the moment of inertia. These materials are not included in the numerical simulation of the rotor casting process; therefore, their properties are presented here for completeness and to provide context for the proposed design concept.

Tungsten heavy alloys based on the W–Ni–Co and W–Ni–Fe systems are multimetallic composites containing a very high tungsten content, typically exceeding 90 wt. %. Their microstructure generally consists of tungsten agglomerates embedded in a ductile metallic binder matrix, which provides the required combination of high strength and sufficient ductility. These materials exhibit a high density ranging from approximately 17.0 to 18.5 g·cm^{-3}, which is significantly higher than that of conventional structural steels and directly contributes to an increase in the moment of inertia of rotating components [24–29].

W–Ni–Co alloys generally exhibit higher strength, hardness and impact toughness. These properties are associated with the beneficial effect of cobalt on the cohesion of the interface between tungsten grains and the metallic binder matrix. The presence of cobalt also promotes greater tungsten solubility in the matrix, contributing to solid-solution strengthening [25,30].

W–Ni–Fe alloys typically exhibit higher ductility and formability while maintaining high density and strength. Due to the presence of iron, these alloys may also exhibit weak ferromagnetic behaviour. From a manufacturing perspective, W–Ni–Fe alloys are generally easier to machine than cobalt-containing alloys [25].

Both material systems exhibit high thermal stability, elevated melting temperatures, and good thermal conductivity. In addition, they provide good resistance to corrosion and structural degradation, primarily due to the dominant tungsten content in their composition [25].

References

1. Xiaojun, L.; Palazzolo, A. A review of flywheel energy storage systems: State of the art and opportunities. *J. Energy Storage* **2022**, *46*, 103576. [CrossRef]
2. Amiryar, M.E.; Pullen, K.R. A Review of Flywheel Energy Storage System Technologies and Their Applications. *Appl. Sci.* **2017**, *7*, 286. [CrossRef]
3. Deng, B. A review of stress analysis on materials and structures for flywheel energy storage systems. *Adv. Eng. Innov.* **2025**, *16*, 84–91. [CrossRef]
4. Dongxu, H.; Xingjian, D.; Wen, L.; Yangli, Z.; Xuehui, Z.; Haisheng, C.; Zhilai, Z. A review of flywheel energy storage rotor materials and structures. *J. Energy Storage* **2023**, *74*, 109076. [CrossRef]
5. Hu, D.; Dai, X.; Xie, B.; Li, W.; Yu, H.; Chen, H. Fatigue Life of Flywheel Energy Storage Rotors Composed of 30Cr2Ni4MoV Steel. *Energies* **2024**, *17*, 3730. [CrossRef]
6. Kale, V.; Secanell, M. A comparative study between optimal metal and composite rotors for flywheel energy storage systems. *Energy Rep.* **2018**, *4*, 576–585. [CrossRef]
7. Bašistová, M.; Radkovský, F.; Lichý, P.; Kielar, Š.; Vasková, I. Numerical Simulation and Optimization of Furnace Roll Casting Production Technology. *Materials* **2025**, *18*, 5445. [CrossRef] [PubMed]
8. Shivtej, S.; Deshpande, J. Casting simulation to identify shrinkage zones & remedies for manufacturing defect free flywheel castings. *Int. J. Sci. Dev. Res.* **2018**, *3*, 226–236.
9. Hebsur, N.S.; Mangshetty, S.J. Casting Simulation for Sand Casting of Flywheel. *IOSR J. Mech. Civ. Eng.* **2014**, *11*, 37–41. [CrossRef]
10. Chen, Z.; Li, Y.; Zhao, F.; Li, S.; Zhang, Z. Progress in numerical simulation of casting process. *Meas. Control* **2022**, *55*, 257–264. [CrossRef]
11. Namchanthra, S.; Suvanjumrat, C.; Chookaew, W.; Wijitdamkerng, W.; Promtong, M. A cfd inves-tigation into molten metal flow and its solidification under gravity sand moul-ding in plumbing components. *Int. J. GEOMATE* **2022**, *22*, 100–108. [CrossRef]
12. Liutyi, R.; Petryk, I.; Mogylatenko, V.; Popovych, V.; Shatska, H. Research Thermal Fields in the Crystallization Process of Steel Cast Parts. *Adv. Mater. Sci. Eng.* **2022**, *2022*, 1–9. [CrossRef]
13. Bertelli, F.; Brito, C.; Meza, E.S.; Cheung, N.; Garcia, A. Inward and outward solidification of cylindrical castings: The role of the metal/mold heat transfer coefficient. *Mater. Chem. Phys.* **2012**, *136*, 2–3. [CrossRef]
14. Yangoz, C.; Erhan, K. High-Speed Kinetic Energy Storage System Development and ANSYS Analysis of Hybrid Multi-Layered Rotor Structure. *Appl. Sci.* **2025**, *15*, 5759. [CrossRef]
15. Růžička, J. Study of the optimization of the casting process for steel flywheel rotors using Magmasoft® simulation software. In *PhD Students' Day FMST 2025*; VSB—Technical University of Ostrava, Faculty of Materials Science and Technology: Ostrava, Czech Republic, 2025; Volume 1, pp. 34–37.

16. Li, K.; Wu, X.; Chen, L.; Chen, D.; Zhu, G.; Shen, Q.; Yoon, J.H. Residual Stress and Microstructure Characterization of 34CrMo4 Steel Modified by Shot Peening. *Scanning* **2020**, *2020*, 1–8. [CrossRef]
17. Zheng, Q.; Li, K.; Yin, X.; Li, B.; Li, C.; Ma, Y.; Sun, J.; Chen, D. Corrosion Properties of 34CrMo4 Steel Modified by Shot Peening. *Scanning* **2017**, *2017*, 1–8. [CrossRef] [PubMed]
18. Dobiáš, M.; Čížek, P.; Kander, L.; Jonšta, P. Hydrogen impact on fracture properties of 34CrMo4 pressure cylinder steel. In Proceedings of the METAL 2023: 32nd International Conference on Metallurgy and Materials, Brno, Czech Republic, 17–19 May 2023; pp. 283–288. [CrossRef]
19. Čížek, P.; Kander, L. Fracture behavior of 34CrMo4 steel in high-pressure hydrogen environment. In Proceedings of the METAL 2020: 29th International Conference on Metallurgy and Materials, Brno, Czech Republic, 20–22 May 2020; pp. 597–602. [CrossRef]
20. Chenakin, S.; Filatova, V.; Makeeva, I.; Vasylyev, M. Ultrasonic impact treatment of CoCrMo alloy: Surface composition and properties. *Appl. Surf. Sci.* **2017**, *408*, 11–20. [CrossRef]
21. Matsunaga, H.; Yoshikawa, M.; Kondo, R.; Yamabe, J.; Matsuoka, S. Slow strain rate tensile and fatigue properties of Cr–Mo and carbon steels in a 115 MPa hydrogen gas atmosphere. *Int. J. Hydrogen Energy* **2015**, *16*, 5739–5748. [CrossRef]
22. Fuentes, A.; Alcântara, N.G.; Rodríguez, S.H.; Ibarra, A.L. Effect of in service weld repair on the performance of CrMo steel steam pipelines. *Mater. Res.* **2006**, *9*, 153–158. [CrossRef]
23. MAGMA GmbH. *MAGMASOFT® [Computer Software]*, Version 6.1; MAGMA GmbH: Aachen, Germany, 2025.
24. Macháčková, A.; Bárta, O.; Brožová, S. Applications of Tungsten Pseudo-Alloys in the Energy Sector. *Appl. Sci.* **2024**, *14*, 647. [CrossRef]
25. Růžička, J. Application of multimetallic composites in FESS technology. In *PhD Students' Day FMST 2024*; VSB—Technical University of Ostrava, Faculty of Materials Science and Technology: Ostrava, Czech Republic, 2024; Volume 1, pp. 33–36.
26. Strunz, P.; Kunčická, L.; Beran, P.; Kocich, R.; Hervoches, C. Correlating Microstrain and Activated Slip Systems with Mechanical Properties within Rotary Swaged WNiCo Pseudoalloy. *Materials* **2020**, *13*, 208. [CrossRef] [PubMed]
27. Pappu, S.; Kennedy, C.; Murr, L.E.; Magness, L.; Kapoor, D. Microstructure analysis and comparison of tungsten alloy rod and [001] oriented columnar-grained tungsten rod ballistic penetrators. *Mater. Sci. Eng.* **1998**, *262*, 115–128. [CrossRef]
28. Růžička, J.; Macháčková, A. Využití kompozitních materiálů na bázi wolframu pro technologické aplikace. *Slévaren. Listy* **2025**, *1*, 29–33. Available online: https://ceskaslevarenska.cz/wp-content/uploads/2025/05/slevarenske_listy_25_1.pdf (accessed on 14 May 2025).
29. Krátká, L.; Petrmichl, R. Stress-Strain Distribution Within Rotary Swaged Tungsten Heavy Alloy. *IOP Conf. Ser. Mater. Sci. Eng.* **2021**, *1190*, 012011. [CrossRef]
30. Macháčková, A.; Brožová, S.; Váňová, P.; Slíva, A.; Konečná, K.; Martynková, G.S. Recyclable Multimetallic High Temperature Materials for Energy Applications. In Proceedings of the METAL 2023: 32nd International Conference on Metallurgy and Materials, Brno, Czech Republic, 17–19 May 2023; pp. 641–646. [CrossRef]